JAAS

ROYAL SOCIETY OF CHEMISTRY

PAPER

View Article Online
View Journal | View Issue

Check for updates

Cite this: *J. Anal. At. Spectrom.*, 2025, **40**, 2016

Published on 16 June 2025. Downloaded on 12/28/2025 7:27:54 PM.

Dual mass spectrometers with plasma-based ion sources for multiplex imaging of elements and biomolecules†

Hui Hsin Khoo, ‡*[a] Ayano Kubota, [b] Takehisa Matsukawa [bc] and Takafumi Hirata [a]

Received 1st February 2025
Accepted 29th May 2025

DOI: 10.1039/d5ja00039d

rsc.li/jaas

Simultaneous imaging analysis of both elements and biomolecules was conducted by the split-flow laser ablation technique using two mass spectrometers equipped with different plasma-based ion sources. The laser-induced sample particles were split into two streams, and introduced into inductively coupled plasma mass spectrometry (ICP-MS) for detection of elements through hard ionisation, and dielectric barrier discharge ionization mass spectrometry (DBDI-MS) for detection of biomolecules through soft ionisation. Selenomethionine was used to optimise the heater current for DBDI-MS and to demonstrate the system's capability for simultaneous detection. The analytical capability of the present technique was demonstrated on mouse brain tissue sections, where elemental maps of Mg, P, Fe, Cu, Zn, and Mo were generated alongside molecular images of lipids and metabolites such as cholesterol, ceramide, sulfatides, and adenine. The imaging results highlighted distinct spatial distributions of elements and biomolecules, correlating them with physiological and structural regions of the brain.

Introduction

Metallomics is a growing omics research area on the study of roles and dynamics of metals and metalloids within biological systems.[1,2] This area of omics complements other omics disciplines such as genomics, proteomics, and metabolomics by elucidating how metals influence biological pathways and molecular functions. Recognising the importance of metals in biological systems, metallomics has emerged to investigate the roles and dynamics of metals and metalloids within these systems. One of the main approaches to study the localisation of metals and metal-containing biomolecules is elemental imaging, which can offer insights into cellular processes and tumour responses to drugs.

Several techniques are widely used for visualising elemental distribution, including micro X-ray fluorescence (μXRF),[3,4] nano-scale secondary ionisation mass spectrometry (nano-SIMS),[5,6] and laser ablation inductively coupled plasma mass spectrometry (LA-ICP-MS).[7–9] Among these techniques, LA-ICP-MS stands out as a robust method due to the high sensitivity and quantitative accuracy, as well as the ability of laser ablation to operate under atmospheric pressure. This not only allows for minimal sample preparation but also preserves the original shape of biological samples, making this technique particularly advantageous for spatially-resolved elemental analysis. While mapping the distribution of elements in biological samples provides valuable insights, combining this information with molecular data can deepen our understanding of the biological context of elements within complex systems.

For the imaging of biomolecules, techniques such as matrix-assisted laser desorption/ionisation mass spectrometry (MALDI-MS),[10,11] time-of-flight secondary ion mass spectrometry (TOF-SIMS),[12,13] and desorption electrospray ionisation mass spectrometry (DESI-MS),[14,15] alongside magnetic resonance imaging (MRI),[16] positron emission tomography (PET),[16] computed tomography (CT),[16] and fluorescence imaging[16] are among the examples. Recently, the integration of multiple imaging techniques, or multimodal imaging, has gained attention to visualise multiple targets in biological samples.[17] In clinical studies, although PET/CT and PET/MRI were applied successfully,[18,19] many earlier multimodal imaging involved molecules, and only the last decade has witnessed advancements in combining multiple imaging platforms for investigation of biomolecules and elements.[20,21] For example, μXRF and MALDI-MS were conducted in tandem to obtain elemental and molecular images.[22,23] The most widely used combined mass spectrometric techniques are LA-ICP-MS and MALDI-MS, applied to various biological samples.[20,24–26]

---

[a] *Geochemical Research Center, Graduate School of Science, The University of Tokyo, Hongo 7-3-1, Bunkyo-ku, Tokyo, 113-0033, Japan. E-mail: h.h.haylie54@gmail.com*

[b] *Faculty of Medicine, Juntendo University, Hongo 2-1-1, Bunkyo-ku, Tokyo, 113-8421, Japan*

[c] *Faculty of Pharmacy, Juntendo University, Hinode 6-8-1, Urayasu, Chiba, 279-0013, Japan*

† Electronic supplementary information (ESI) available. See DOI: **https://doi.org/10.1039/d5ja00039d**

‡ Present address: BioChromato Inc., 1-12-19 Honcho, Fujisawa, Kanagawa, 251-0053, Japan.

This journal is © The Royal Society of Chemistry 2025

Published on 16 June 2025. Downloaded on 12/28/2025 7:27:54 PM.

Due to differences in analytical principles, most multimodal imaging techniques are conducted separately. When a non-destructive technique is involved, the same sample can be reused for subsequent analysis to derive elemental/molecular information. However, the major challenge lies in achieving reproducible sample mounting when transferring the sample between instruments. In contrast, for techniques involving destructive analyses, different sections of the same biological sample are typically prepared for each technique. Comparison of the resulting images is generally conducted by visually overlaying the images generated from different techniques. This approach can complicate the correlation of final images, especially for heterogeneous samples. For instance, in a study analysing tumour samples treated with the Pt-based anticancer drug cisplatin using LA-ICP-MS and MALDI-MS, cisplatin (Pt) was only able to be imaged by LA-ICP-MS. In contrast, MALDI-MS failed to detect any known drug-related molecules,[24] making it difficult to draw conclusions regarding the drug's penetration into the tumour tissue. Determining the cause of this non-detection can be difficult, because it is unknown whether it resulted from signal suppression caused by the matrix used in MALDI-MS or from sample heterogeneity.

This has led to the development of analytical techniques using a single sampling source for simultaneous acquisition. For instance, laser induced breakdown spectroscopy (LIBS) and LA-ICP-MS were combined into a single instrument, utilising a shared laser source to analyse major and trace elements in geological samples.[27] For combined elemental and molecular analysis, Herdering *et al.* demonstrated a method where laser ablation aerosols were divided into two streams, enabling the analysis of kidney and lymph node samples with ICP-MS and atmospheric pressure chemical ionisation mass spectrometry (APCI-MS).[28] Another example was reported by Paing *et al.*, where they combined laser ablation with a single ion source, liquid sampling-atmospheric pressure glow discharge plasma (LS-APGD) for simultaneous acquisition of elemental and molecular data.[29] While these approaches are useful for the detection of elemental and molecular information at the same time, further improvements are needed to enhance the practicality for analysing complex samples. For example, in LA-ICP-MS/APCI-MS analysis,[28] molecular detection was limited to analytes with high concentrations, possibly due to the reduced sensitivity in molecular analysis. In the case of LA-LS-APGD, using a single ion source for both elemental and molecular detection requires careful optimisation of parameters such as the interelectrode gap, discharge current, and the choice of solvent electrolytes.[29,30]

In this study, we adopted an approach similar to that of Herdering *et al.*, integrating laser ablation with ICP-MS and dielectric barrier discharge ionisation mass spectrometry (DBDI-MS) for concurrent elemental and molecular imaging. Here, DBDI was used as the ion source for molecular detection because it operates with a larger discharge current compared to APCI, which is expected to provide a higher ionisation capacity. The DBDI used in this study has a high-frequency current limiter integrated into the AC power supply. This can obviate the risk of causing an arc discharge, which could lead to unstable ionisation. The LA-ICP-MS/DBDI-MS setup was previously described in our earlier publication.[31] However, the present study employed a time-of-flight mass spectrometer for molecular analysis to enable high-resolution mass detection of analytes from complex samples. This approach was initially demonstrated by optimising parameters using selenomethionine as a model compound, which served as a representative example for simultaneous elemental and molecular analysis. Its application to bioimaging was further validated with a single tissue section from a mouse brain. The results underscore the potential of this technique to provide complementary elemental and molecular information from a single sample, offering significant advantages for studying complex biological systems.

Experimental

Chemicals and materials

The following reagents were purchased: phosphorus standard solution (Kanto Chemical Co., Inc), L-selenomethionine, glycerol, ethylene glycol (Nacalai Tesque Inc., Kyoto, Japan), copper standard solution, 4-aminobutanoic acid (also known as γ-aminobutyric acid, GABA), adenine, glutamic acid, cholesterol, L-α-phosphatidylcholine (dipalmitoyl) (FUJIFILM Wako Pure Chemical Industries, Ltd, Osaka, Japan), dopamine hydrochloride (LKT Labs. Inc), adenosine 5′-diphosphate, sulfatides from bovine brain (Sigma Aldrich), and ceramide (brain, porcine) (Avanti Research). No further purification procedures were performed in this study. For GABA, adenine, glutamic acid, selenomethionine, cholesterol, dopamine hydrochloride, and adenosine 5′-diphosphate, approximately 50 mg of each reagent was pressed into powder pellets using a hydraulic press (PIKE Technologies, Madison, USA) at a pressure of 2.55 MPa.

Selenomethionine was used for system optimisation in this study due to the presence of selenium in the compound, enabling simultaneous monitoring of both elemental and molecular signal responses. Selenomethionine pellet was used to optimise heater temperature and gas flow. To demonstrate the capability of LA-ICP-MS/DBDI-MS for simultaneous acquisition, selenomethionine was diluted with MilliQ (ultrapure) water (Millipore, MA, USA) to a concentration of 1 mg mL^{-1}, and the solution was dropped onto a glass slide. The droplet was dried using a hot plate set to 70 °C to form crystals.

For validation of the analytes contained in mouse brain, standard solutions of phosphorus and copper were diluted in MilliQ water to a final concentration of 1 μg mL^{-1} as a representative of elemental analytes of interest. Molecular analytes such as cholesterol, L-α-phosphatidylcholine (dipalmitoyl), ceramide, and sulfatide were diluted in 2 : 1 chloroform/methanol to a final concentration of 1 mg mL^{-1}. All solutions were deposited into 2 mm-diameter wells of a Teflon-printed glass slide. The droplets were left to dry before analysis.

Instrumentation

The laser ablation system utilised in this study was a Yb:KGW femtosecond laser equipped with galvanometric mirrors, operating at a wavelength of 260 nm and a pulse duration of 290 fs (Jupiter Solid Nebulizer, ST Japan, Tokyo, Japan). Laser-induced

Published on 16 June 2025. Downloaded on 12/28/2025 7:27:54 PM.

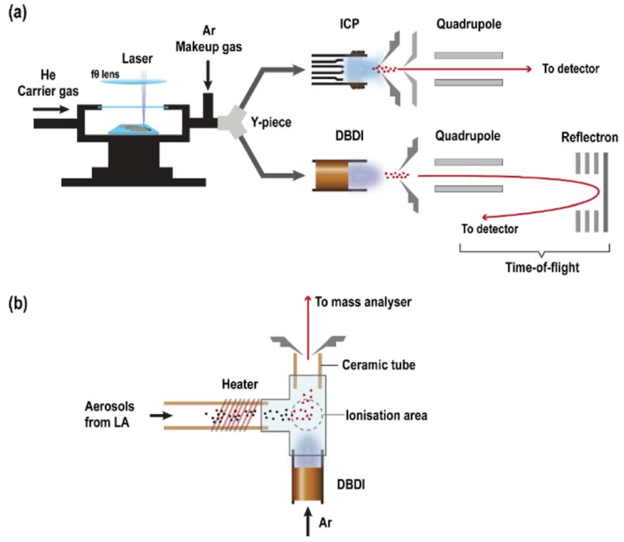

Fig. 1 Schematic diagram of the (a) instrumental setup for simultaneous analysis of elements and molecules and (b) LA-DBDI-MS.

aerosols were divided into two streams *via* the split flow technique using a Y-piece. The sample particles were then introduced into two mass spectrometers with different ion sources, (i) ICP-MS and (ii) DBDI-MS, in parallel to detect elements and molecules, respectively. The instrumental setup is shown in Fig. 1(a). For the detection of elements, a triple quadrupole-based ICP-MS (NexION 5000, PerkinElmer, Shelton, CT, USA) was used. For DBDI-MS, a hybrid quadrupole time-of-flight mass spectrometer (Xevo G2-XS QTof, Waters Corporation, MA, USA) equipped with an in-house DBDI, utilising Ar as plasma gas, was employed. A T-shaped glassware connected the ion source, heater, and the mass spectrometer. Aerosols produced by laser ablation were heated to promote analyte desorption prior to ionisation through proton transfer. Details of this ion source can be found in our previous work.[32] Note that the configuration of the DBDI and the organic mass spectrometer differed from our previous work due to a change in the orientation of the mass spectrometer interface (Fig. 1(b)). Instrumental settings were optimised with selenomethionine through the monitoring of the signal intensity of ^{77}Se for ICP-MS and protonated ion of the compound at a mass-to-charge ratio (m/z) 195.01 for DBDI-MS. Detailed instrumental and experimental parameters are summarised in Table 1.

Heater current optimisation

A selenomethionine pellet was used for heater current optimisation in DBDI-MS. The parameter was optimised using LA-DBDI-MS alone (Fig. 1(b)) before coupling with ICP-MS. A single run consisted of a 30-second gas blank, followed by 15 seconds of laser ablation on a 150 × 150 μm sampling area. Data acquisition was conducted with a scan time of 1 second.

Tissue sectioning

Animal experiments were approved by the Animal Care and Use Committee of UNITECH Co. Ltd. (Kashiwa, Japan) (approval number: AGR TD-241115A-27) and conducted at UNITECH in accordance with the guidelines. Eight-week-old male S1c:ICR mice (Japan SLC, Inc., Shizuoka, Japan) were used in this study. All animals were euthanised by exsanguination under deep isoflurane anaesthesia, followed by perfusion with 4% paraformaldehyde phosphate buffer solution (4% PFA PBS; FUJIFILM Wako Pure Chemical Corporation, Osaka, Japan) for tissue fixation. Brains were then collected and post-fixed in 4% PFA.

The fixed brain tissues were subjected to stepwise cryoprotection by immersion in sucrose solutions of increasing concentrations: 10% sucrose/PBS for two hours, 20% sucrose/PBS for six hours, and 30% sucrose/PBS for 48 hours. The cryoprotected tissues were embedded in M1 embedding matrix (Thermo Fisher Scientific, MA, USA) and sectioned into 50 μm slices using a Leica CM3050 S microtome (Leica Microsystems, Wetzlar, Germany). The tissue sections were stored at −20 °C in an antifreeze solution containing 25% glycerol and 30% ethylene glycol in PBS. There was a few weeks' interval between tissue preparation and imaging. No staining procedures were made on the analysed sample.

Data acquisition for imaging analysis

Imaging analysis was conducted by repeated line-scanning of the laser beam. The 10 μm laser beam was set to partially overlap with each other due to its Gaussian nature, and ablation followed a “pseudo-line” pattern, where the vertical length was 50 μm, defining the vertical spatial resolution. The horizontal spatial resolution depended on the mass scan for one cycle, raster speed, and repetition rate. The raster speed for a single pseudo-line was 50 μm s^{-1}, with no gap between each line. A 30-second blank signal was obtained before laser irradiation on the sample.

Signal intensity profiles were acquired based on time-resolved analysis (displayed as total ion chromatogram, TIC, for the organic mass spectrometer). Data acquisition was conducted under the following conditions: dwell time of 30 ms for all elements except ^{78}Se (100 ms) and ^{98}Mo (200 ms) for ICP-MS. The RPa values (DC voltage of the Universal Cell) were deliberately detuned for highly abundant elements, such as ^{13}C, ^{31}P, and ^{34}S, to reduce sensitivity of these elements and prevent detector saturation. For DBDI-MS, experimental conditions of a scan rate of 0.2 seconds per mass spectrum and a scan range of 50–1200 Da were used. Acquisition of the right hemisphere of the mouse brain was performed in negative mode, while the left hemisphere was acquired in positive mode for the DBDI-MS images. ICP-MS images were acquired for both hemispheres. A single coronal section of brain tissue was used for the analysis.

Data processing

For elemental analysis, the imaging data of selected elements were exported as comma-separated values (CSV) formatted files. For molecular analysis, the average mass spectrum of a single line on the sample was first obtained, and specific m/z values were selected to display extracted ion chromatograms (EICs)

This journal is © The Royal Society of Chemistry 2025

Published on 16 June 2025. Downloaded on 12/28/2025 7:27:54 PM.

Table 1 Instrumentation and operational settings

Laser ablation system	
Instrument	Jupiter solid nebulizer (ST Japan)
Laser source	Yb:KGW
Wavelength	260 nm
Pulse duration	290 fs
Fluence	0.8 J cm^{-2} (selenomethionine) 1.5 J cm^{-2} (imaging)
Repetition rate	100 Hz (selenomethionine) 2000 Hz (imaging)
He gas (carrier gas)	0.6
Ar gas (makeup gas)	2.4
Imaging conditions	Vertical spatial resolution: 50 μm Scan speed: 50 μm s^{-1} Number of lines: 115 Time interval between lines: 20 s
ICP-MS	
Instrument	NexION 5000 (Perkin Elmer) (quadrupole)
ICP forward power	1600 W
Coolant gas	16.0 L min^{-1}
Auxiliary gas	1.2 L min^{-1}
Acquisition mode	He-KED mode (selenomethionine) Standard mode (no gas) (imaging)
Collision gas (for KED)	He gas (4.0 mL min^{-1})
Detector	Electron multiplier
Detection system	Pulse counting/Analog
Monitored isotopes	$^{74-82}Se$ (selenomethionine) ^{13}C, ^{25}Mg, ^{31}P, ^{34}S, ^{55}Mn, ^{57}Fe, ^{65}Cu, ^{67}Zn, ^{78}Se, ^{98}Mo (imaging)
Dwell time	50 ms (selenomethionine) 30 ms for all ions except for ^{78}Se (100 ms) and ^{98}Mo (200 ms) (imaging)
Organic MS	
Instrument	Xevo G2-XS (Waters Corporation)
Gas flow	Cone gas: 0 L h^{-1}; desolvation gas: 0 L h^{-1}
Acquisition mode	MS scanning
Ion polarity	Positive (selenomethionine) Negative (right hemisphere) and Positive (left hemisphere) for imaging
Detector	Electron multiplier
Detection system	Pulse counting
Mass range	50–1200 Da
Scan time	0.4 s (selenomethionine), 0.2 si(Imaging)
Ion source	In-house DBDI
Plasma gas	0.6 L min^{-1}
Heater current	3.0 a

(range: extracted $m/z \pm 0.01$ Da). EICs for each m/z were exported as text (TXT) files and then converted into CSV format. Both data sets were imported into BioQuant for data processing and image construction.

BioQuant is a newly-developed software that processes data from two separate mass spectrometers within a single user interface.[32] This software can correct for differences in the starting times of the elemental and molecular signals. The timing difference in the signal rise was caused by starting each mass spectrometer at different times. The software can also redefine the spatial resolution of one pixel. The dimension of one pixel in the horizontal direction could be adjusted to ensure compatibility between the data sets. The vertical spatial resolution remained the same, while the horizontal spatial resolution, defined by the mass scan for one cycle, varied for each mass spectrometer due to the different mass scan timings. This discrepancy resulted in different spatial resolutions for the elemental and molecular images, complicating pixel-by-pixel comparison. Before correction, the horizontal resolutions for elemental and molecular data were 37 μm and 11 μm, respectively. After correction, one pixel was redefined as 72 μm × 50 μm (horizontal (x) × vertical (y) directions) for both data sets.

Results and discussion

Heater current optimisation

Selenomethionine was initially analysed using laser ablation connected only to DBDI-MS (Fig. 1(b)) to investigate its ionisation characteristics and to determine the optimal heater current for analyte desorption. During laser ablation, a mixture of gas molecules and particles is transported from the ablation cell to the plasma for ionisation. While ionisation occurs when

Published on 16 June 2025. Downloaded on 12/28/2025 7:27:54 PM.

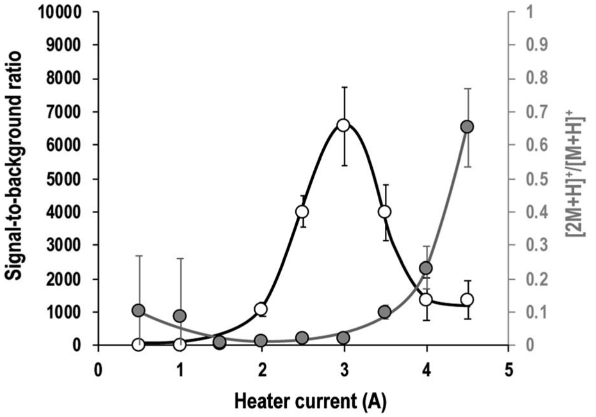

Fig. 2 Signal-to-background ratio of *m/z* 198.00 (white plots), and the ratio of the protonated dimer (*m/z* 394.96) to the protonated molecules (*m/z* 198.00) (gray plots), measured using LA-DBDI-MS at various heater currents. Error bars represent 2SD ($N = 5$).

sufficient energy is applied to the sample, the process will be more efficient when more molecules are present in the gas phase compared to when molecules are in the bulk phase (particles). The desorption process, which involves the release of intact molecules from the bulk into the gas phase, benefits DBDI due to its capability of forming ions in the gas phase, and thus enhance ionisation efficiency. Studies suggest that thermal processes play a significant role in desorption.[30,33–35] To promote desorption and enhance ionisation efficiency, we used a heater in the analyte pathway before ionisation occurs.

Ions detected at *m/z* 198.00 (protonated molecule of ^{80}Se in selenomethionine) were used to optimise the heater current. The white plots in Fig. 2 illustrate the relationship between the signal-to-background ratio and heater current. As the heater current increased, analyte intensity also increased, reaching the highest signal-to-background ratio at 3 A. However, beyond this point, the ratio began to decline. This decrease is attributed to the increased formation of protonated dimers (Fig. 2 gray plots), whose intensity also increased with heater current. These results suggest that elevated currents generate more thermal energy, enhancing the desorption process by releasing more molecules from particles and improving ionisation efficiency. However, excessive heat can lead to greater dimer formation, which may complicate the interpretation of the mass spectrum. Therefore, while sufficient heat is essential for effective desorption, excessively high currents should be avoided.

Simultaneous detection from both mass spectrometers

Fig. 3 shows the results of LA-ICP-MS/DBDI-MS for the analysis of selenomethionine. The mass spectra obtained using ICP-MS displayed the isotopic composition of selenium, reflecting its natural abundance (Fig. 3(a)). For DBDI-MS, both the protonated molecule $[\mathrm{M+H}]^+$ of selenomethionine and a fragment ion $[\mathrm{M-NH_3+H}]^+$ were observed (Fig. 3(c)). All peaks showed a mass deviation within ±10 ppm between the calculated and detected exact masses. The signal intensity profiles demonstrated the simultaneous acquisition of both elements and molecules (Fig. 3(b) and (d)). ^{77}Se and *m/z* 195.01 (protonated molecule of selenomethionine containing ^{77}Se) were tracked as time-resolved data during laser ablation on a selenomethionine droplet. Both profiles exhibited a similar pattern, indicating the feasibility of simultaneous measurement. These results highlight the complementary capabilities of ICP-MS and DBDI-MS in the simultaneous analysis of elements and molecules. This

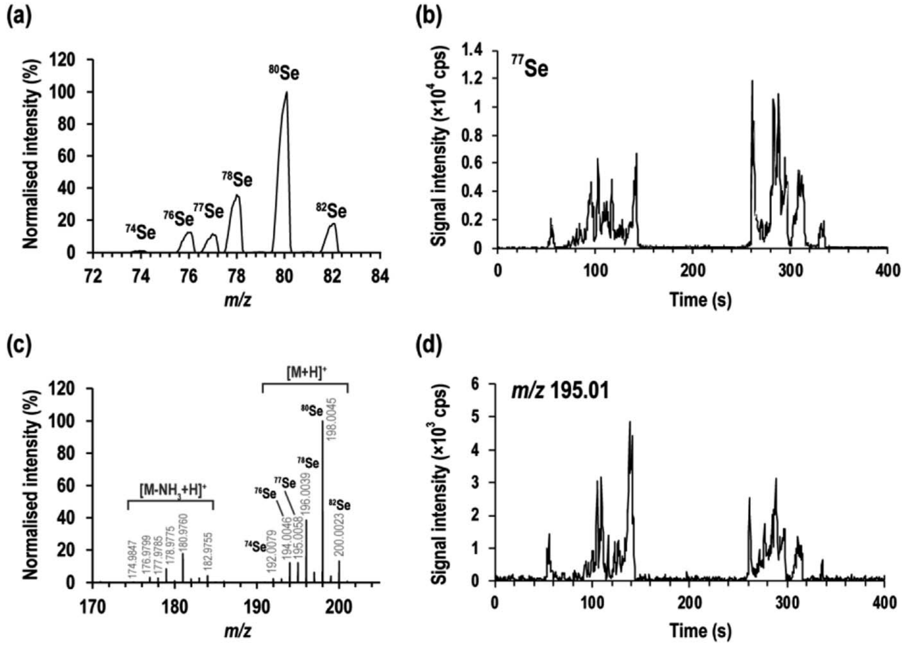

Fig. 3 Detection of selenomethionine using the LA-ICP-MS/DBDI-MS system. (a) Mass spectrum of selenium obtained from ICP-MS and (b) the corresponding signal intensity profile recorded for a single line across a selenomethionine droplet. Similarly, (c) the mass spectrum of selenomethionine obtained from DBDI-MS and (d) its signal intensity profile recorded along the same line.

This journal is © The Royal Society of Chemistry 2025

Published on 16 June 2025. Downloaded on 12/28/2025 7:27:54 PM.

suggests that the present system holds potential for future studies on the chemical forms of elements in various samples.

Spatial mapping and analytical validation of target analytes in mouse brain tissue

To demonstrate the simultaneous elemental and molecular imaging capabilities of the current system, a mouse brain section was analysed. The brain is a highly complex organ composed of a wide variety of chemical substances that support its structure and function, including neurotransmitters, proteins, peptides, lipids, metabolites, nucleotides, and metal ions.[36–38] The present imaging analysis aimed to assess whether this analytical approach could be applied to such a complex sample. The resulting images are shown in Fig. 4. For biomolecular images, the right

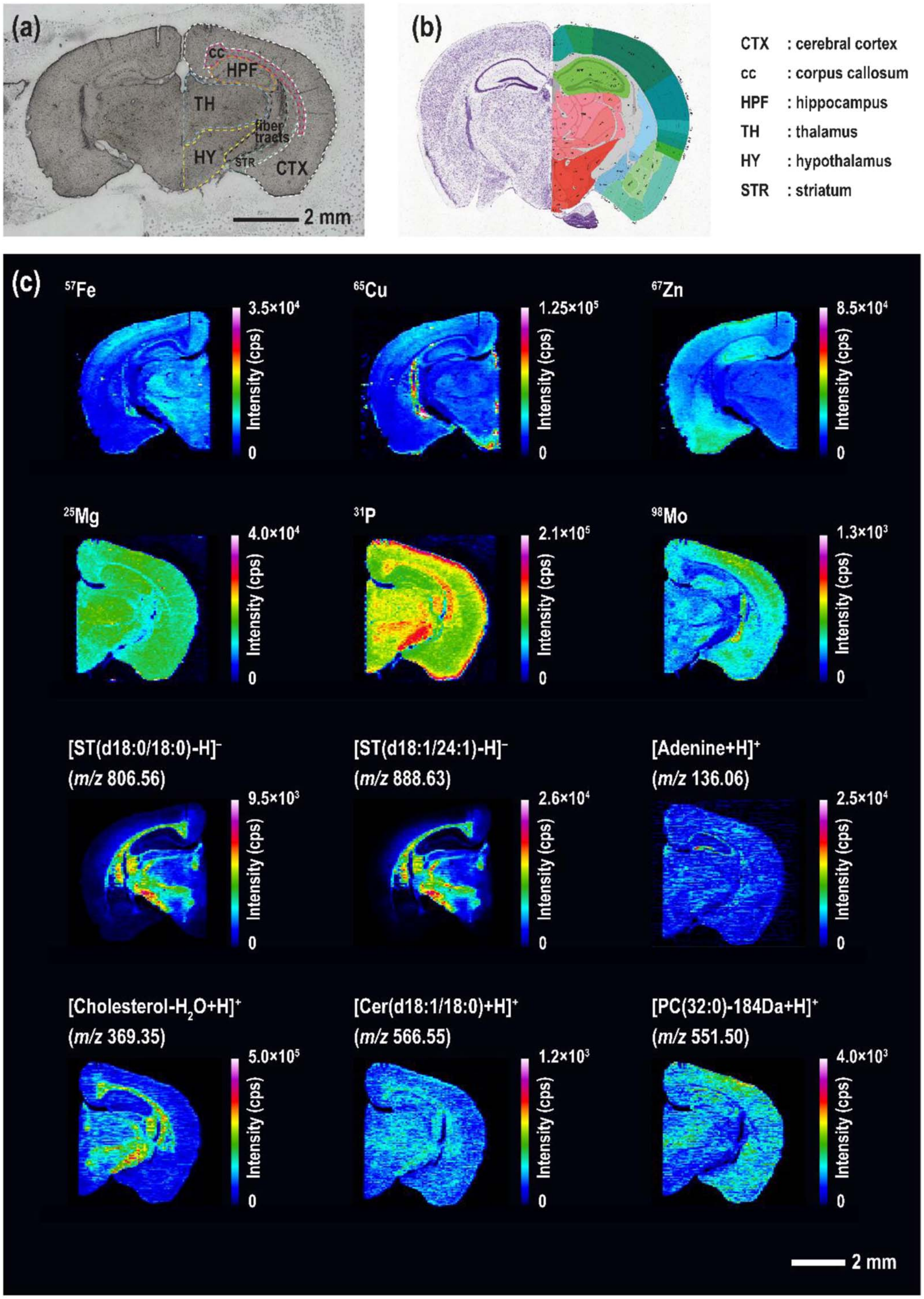

Fig. 4 Optical image and MS images of a coronal mouse brain section. (a) Optical image of the analysed brain section. The parts of the brain were labelled with reference to the (b) Allen Brain Atlas (#74 in Coronal Atlas). (c) Imaging results of elements and biomolecules.

Published on 16 June 2025. Downloaded on 12/28/2025 7:27:54 PM.

hemisphere of the brain was obtained in negative ion mode, while the left hemisphere was acquired in positive ion mode.

Non-metals (such as P) and essential trace metals (such as Mg, Fe, Cu, Zn, and Mo) were detected. All elements exhibited heterogeneous distributions within the brain. Magnesium was distributed relatively homogeneously throughout the brain, with lower abundances observed in the corpus callosum and fiber tracts (*i.e.*, white matter). Phosphorus was found to be enriched in the corpus callosum and cerebral peduncle, while iron was concentrated in the pyramidal layers of the hippocampus. Copper was predominantly concentrated in the ventricular systems. Zinc, in contrast, was primarily localised in the CA3 region of the hippocampus (particularly in the stratum lucidum), amygdala, and specific areas of the cerebral cortex. Our results were consistent with the images reported from previous studies.[39,40] In addition, we were able to image molybdenum, which was seldom reported. This element was present in the cerebral cortex, dentate gyrus, CA3 area of the hippocampus, and fiber tracts. Studies on the localisation of molybdenum are limited; however, research indicates that molybdenum acts as a cofactor for the activation of enzymes such as sulfite oxidase, aldehyde oxidase, xanthine oxidase, and mitochondrial amidoxime reducing component.[41,42] This suggests that molybdenum may play a role in reducing reactive intermediates such as sulfite and aldehydes, thereby minimising the generation of reactive oxygen species that can damage neurons. Notably, the hippocampus, which is rich in neurons, may particularly benefit from this protective function.

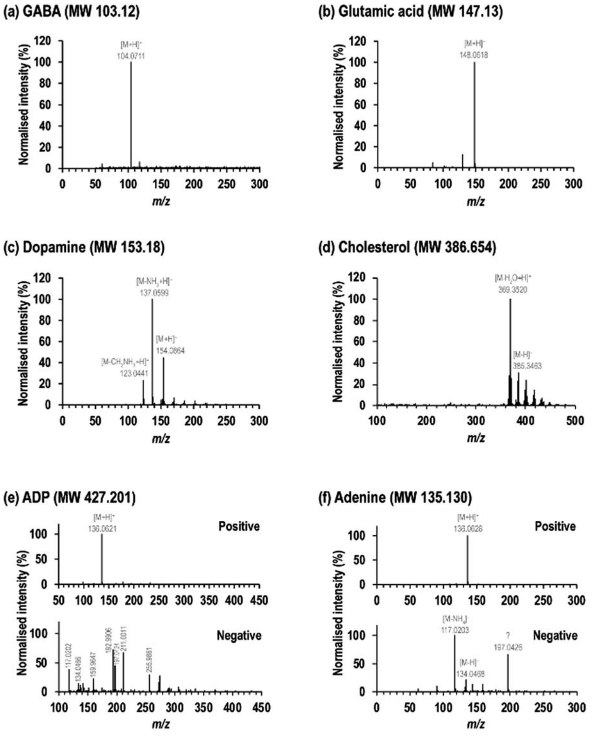

Fig. 5 Mass spectra of (a) GABA, (b) glutamic acid, (c) dopamine, (d) cholesterol, (e) ADP in positive and negative ion modes, and (f) adenine in positive and negative ion modes. All analytes were analysed with LA-DBDI-MS only (Fig. 1(b)).

Biomolecular ions were identified by comparing results with reagents analysed (Fig. 5) and with findings from previous research. For instance, *m*/*z* 136.06 was assigned to the protonated ion of adenine, consistent with the adenine reagent analysed in positive ion mode (Fig. 5(f)). However, it is also plausible that *m*/*z* 136.06 represents a fragment of adenosine triphosphate (ATP), adenosine diphosphate (ADP), or adenine monophosphate (AMP), as observed in the analysis of the ADP reagent, where *m*/*z* 136.06 was detected (Fig. 5(e) positive).

Lipids were also detected. *m*/*z* 806.60 and *m*/*z* 888.62 were assigned as the deprotonated molecules of sulfatides. In positive ion mode, *m*/*z* 369.35 and *m*/*z* 566.55 were attributed to cholesterol and ceramide (Cer(d18 : 1/18 : 0)), detected as $[M-H_2O+H]^+$ and $[M+H]^+$, respectively. Cholesterol and sulfatides were highly concentrated in the white matter region, particularly in the corpus callosum and fiber tracts, where bundles of myelinated axons are densely populated. Ceramide (Cer (d18 : 1/18 : 0) was relatively distributed evenly throughout the brain, with slightly high abundance in the hippocampus and olfactory areas. These results were in good agreement with the reported literature on the distribution of lipids in mouse brain tissue.[43–46] Additionally, *m*/*z* 551.50 was tentatively assigned as a fragment of phosphatidylcholine (PC(32 : 0)). This ion showed a distribution contrasting cholesterol and sulfatides, mainly localising in gray matter. Previous studies using APCI-MS for phospholipid detection reported the detection of diacylglyceride (DAG) fragments due to the loss of the phosphate-containing head group.[47,48] Since DBDI shares a similar ionisation mechanism with APCI,[49,50] it is likely that a similar phenomenon occurred in this study. Given that PC constitutes the majority of phospholipids,[51] it is highly probable that *m*/*z* 551.50 originated from PC. However, the possibility that *m*/*z* 551.50 represents isomers from other phospholipid fragments cannot be excluded.

Among the images, iron displayed a similar pattern to *m*/*z* 136.06 (proposed as adenine or a fragment of ATP, ADP, or AMP), both concentrated in pyramidal layers of the hippocampus. The hippocampus requires significant energy to maintain neuronal function, and mitochondria play a central role in Fe utilisation and ATP production. Iron is present in iron–sulphur clusters and cytochrome c, which mediate electron transfer within mitochondria, leading to the synthesis of ATP. Phosphorus was also observed to be enriched in the same regions as *m*/*z* 136.06 in the hippocampus, which may further support the hypothesis of *m*/*z* 136.06 originating from nucleotides (*e.g.*, ATP, ADP and AMP). However, phosphorus was also distributed in the white matter (*i.e.*, corpus callosum and fiber tract) and certain areas in the cerebral cortex. In contrast, PC(32 : 0) displayed an opposite trend. This may seem counterintuitive, as phosphorus is a component in phosphatidylcholine. However, phosphorus is also found in other biomolecules, such as nucleotides, nucleic acids (DNA and RNA), phosphorylated proteins, and phospholipids other than PC(32 : 0). These biomolecules are often more abundant in metabolically active regions of the brain, where cellular activities and energy production are intense, which may explain the observed distribution.

To confirm the identity of the analytes detected, additional validation analysis was performed to ensure accurate

Published on 16 June 2025. Downloaded on 12/28/2025 7:27:54 PM.

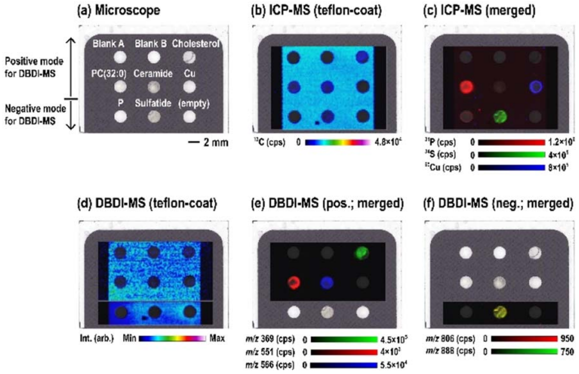

Fig. 6 Mapping of several analytes of interest. (a) Optical image of the glass slide after analyte deposition. Blank A contains MilliQ water and Blank B contains a chloroform/methanol mixture. (b)–(c) Elemental maps from ICP-MS: (b) Teflon coating (^{13}C) and (c) analytes showing ^{31}P, ^{34}S, and ^{65}Cu. (d)–(f) Molecular maps from DBDI-MS: (d) Teflon coating detected at *m*/*z* 199.07 (positive mode) and *m*/*z* 185.92 (negative mode), (e) molecular analytes detected in positive mode including cholesterol (*m*/*z* 369.35), PC(32 : 0) (*m*/*z* 551.50), and ceramide (*m*/*z* 566.55), and (f) sulfatides detected in negative mode at *m*/*z* 806.57 and *m*/*z* 888.64. (c), (e), and (f) show merged ion images of multiple analytes.

identification. Based on the predicted analytes detected in the mouse brain, reagents were selected and purchased for validation. These reagents were prepared as solutions and deposited onto a glass slide with a Teflon coating. The imaging results are shown in Fig. 6. All analytes showed good correlation with the spatial patterns observed in the optical image (Fig. 6(a)). In addition, for analytes containing both elemental and molecular components, such as PC(32 : 0) (which contains phosphorus) and sulfatides (which contain sulphur), the elements exhibited distributions identical to their molecular counterparts: phosphorus and PC(32 : 0) showed a higher signal intensity along the circumference of the residue, while sulphur and sulfatides displayed a distinctive creased pattern in the residue. These results, alongside the mass spectra obtained for these analytes (Fig. S1†), support our predictions regarding the assigned peaks in Fig. 4.

The limit of detection (LOD) for the present LA-ICP-MS/DBDI-MS technique was determined based on the mean of the background signal plus three times the standard deviation of the background signal. For ICP-MS, the calculated LODs were 6.5 pg for phosphorus, 0.4 pg for copper, and 2.4 pg for zinc. As for DBDI-MS, the LODs were 91 pg for adenine (*m*/*z* 136.06), 97 pg for cholesterol (*m*/*z* 369.35), and 698 pg for PC(32 : 0) (*m*/*z* 551.50).

Correlation analysis is one of the principal methods to understand the potential interactions among components. Correlation analyses conducted in previous studies are mostly either only among elements[52] or biomolecules.[53] In contrast, with the present multiplex imaging technique, correlation analysis based on both elements and biomolecules could be made. Fig. 7 presents the correlation analysis of ^{31}P, ^{57}Fe, and *m*/*z* 136.06. The analysis focused on the region surrounding CA1 and CA2 pyramidal layers of the hippocampus, where all three analytes colocalised. The results indicated positive correlations between these three components. This enhances the accuracy of multi-analyte correlation by ensuring that all analytes are evaluated at the same spatial resolution, and hence improving the reliability of biological interpretation.

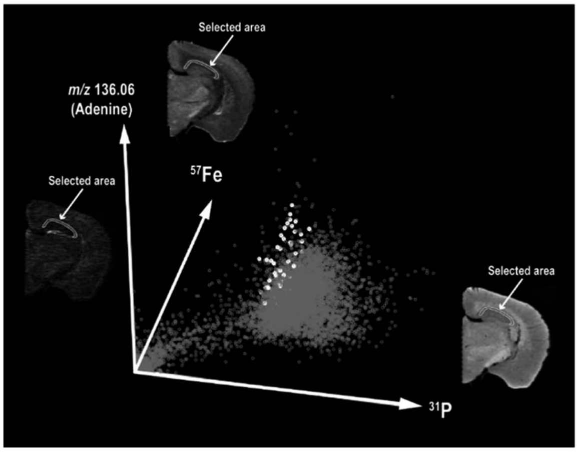

Fig. 7 Correlation analysis of ^{31}P, ^{57}Fe, and *m*/*z* 136.06 (adenine). The brain region outlined in white represents the selected area for correlation analysis. The corresponding data points within this area are displayed as white plots.

Neurotransmitters such as GABA, glutamic acid, and dopamine reagents were analysed (Fig. 5(a)–(c)) due to these substances being reported to have interactions with metal ions such as Fe, Cu, and Zn.[54] GABA and glutamic acid were observed as protonated molecules at *m*/*z* 104.07 and *m*/*z* 148.06, respectively, while dopamine was primarily detected as a deaminated fragment ion at *m*/*z* 137.06. These neurotransmitters were successfully imaged using techniques such as MALDI-MS, laser ablation electrospray ionisation mass spectrometry (LAESI-MS), and DESI-MS,[11,15,55] but unfortunately, they were not detected in this study. Dopamine, which is mainly concentrated in the medulla oblongata, was not observed because this brain structure was not included in the prepared brain section. Another likely reason for the lack of detection is the low sensitivity of the molecular detection system. Neurotransmitters such as GABA, dopamine, serotonin, acetylcholine, norepinephrine, and so on typically exist in concentrations ranging from nM to μM.[56] To address this limitation, further improvements in sensitivity are required to detect low-concentration analytes.

For lipids, a peak at *m*/*z* 834, predicted to be phosphatidylserine (PS), was detected. However, its distribution differed from that of phosphatidylserine PS (18 : 0/22 : 6) reported in a previous study.[14] While this lipid is known to be abundant in grey matter, our results showed a distribution more similar to the sulfatides, which are concentrated in white matter. Therefore, this suggests that PS was not detected as the $[M-H]^-$ ion in this study. Similarly, the identification of phospholipids including phosphatidylethanolamine, phosphatidylinositol, and sphingomyelin requires further analysis of the reagents. To achieve more comprehensive identification of the compounds present, additional fundamental research on the ionisation characteristics of various analytes using DBDI-MS is necessary.

Published on 16 June 2025. Downloaded on 12/28/2025 7:27:54 PM.

The averaged mass spectrum of a single line from the sample revealed a wealth of sample-related compounds. The ions shown here represent only a fraction of the full spectrum and provide just a glimpse into the sample's complexity.

Given the growing interest in omics technologies, this multiplex approach provides the opportunity to combine multiple types of data (*i.e.*, metallomics, lipidomics, and metabolomics) to gain deeper insights into physiological processes and pathophysiological changes in brain diseases. By integrating such data, this method could offer a comprehensive understanding of the brain's chemical environment and its alterations under various conditions. Additionally, resources such as the Allen Brain Atlas can play a pivotal role in achieving this goal by providing a detailed reference of brain structure and gene expression, enabling better correlation of omics data with anatomical data.

Conclusions

This study successfully demonstrated the combination of LA-ICP-MS with DBDI-MS for simultaneous elemental and molecular imaging from a single sample. Selenomethionine served as a proof-of-concept for the system's ability for simultaneous detection and the possibility to analyse the chemical forms of metals, whether in free form or as part of a compound. Application to mouse brain tissue revealed distinct yet interconnected patterns of elements and biomolecules. While the system proved effective for analysing lipids and certain biomolecules, challenges such as the detection of low-abundance biomolecules were noted, requiring further sensitivity improvements. Overall, the present technique represents another candidate for comprehensive analysis of complex biological systems, with potential applications in exploring physiological processes, disease mechanisms, and therapeutic targets.

Data availability

The data supporting this article have been included as part of the ESI.†

Author contributions

H. H. K. and T. H. designed the study. H. H. K. carried out the experiments and conducted data processing. A. K. and T. M. supervised the animal experiments and prepared the brain tissue sections. H. H. K. wrote the manuscript. T. H. supervised the study and acquired funding. All authors discussed the results and reviewed the manuscript.

Conflicts of interest

There are no conflicts to declare.

Acknowledgements

We thank Dr Toshihiro Suzuki (the University of Tokyo) for developing the BioQuant software, giving advice on software operation, and critically reading the manuscript, Dr Hidekazu Miyahara (the University of Tokyo) for offering technical support on the DBDI source, Dr Shuji Yamashita (Doshisha University) for technical support of the instruments and scientific advice, Haruo Shimada and Takao Nishiguchi (Bio-Chromato Inc.) for fabricating the ion source interface, Chihaya Kinoshita and Zixin Han (the University of Tokyo) for technical support of ICP-MS. This work was financially supported by Grant-in-Aid for Scientific Research (JP21H04511) from the Ministry of Education, Culture, Sports, Science and Technology, Japan.

References

1 H. Haraguchi, *J. Anal. At. Spectrom.*, 2004, **19**, 5–14.
2 H. Haraguchi, *Metallomics*, 2017, **9**, 1001–1013.
3 B. De Samber, G. Silversmit, K. De Schamphelaere, R. Evens, T. Schoonjans, B. Vekemans, C. Janssen, B. Masschaele, L. Van Hoorebeke, I. Szalóki, F. Vanhaecke, K. Rickers, G. Falkenberg and L. Vincze, *J. Anal. At. Spectrom.*, 2010, **25**, 544–553.
4 P. M. Wróbel, S. Bała, M. Czyzycki, M. Golasik, T. Librowski, B. Ostachowics, W. Piekoszewski, A. Surówka and M. Lankosz, *Talanta*, 2017, **162**, 654–659.
5 A. A. Legin, A. Schintlmeister, M. A. Jakupec, M. S. Galanski, I. Lichtscheidl, M. Wagner and B. K. Keppler, *Chem. Sci.*, 2014, **5**, 3135–3143.
6 J. Malherbe, F. Penen, M.-P. Isaure, J. Frank, G. Hause, D. Dobritzsch, E. Gontier, F. Horréard, F. Hollion and D. Schaumlöffel, *Anal. Chem.*, 2016, **88**, 7130–7136.
7 Y. Makino, S. Ohara, M. Yamada, S. Mukoyama, K. Hattori, S. Sakata, Y. Tanaka, T. Suzuki, A. Shinohara, T. Matsukawa, K. Yokoyama, and T. Hirata, in *Metallomics: Recent Analytical Techniques and Applications*, ed. Y. Ogra and T. Hirata, Springer, Tokyo, 2017, pp. 93–106.
8 S. Yamashita, Y. Yoshikuni, H. Obayashi, T. Suzuki, D. Green and T. Hirata, *Anal. Chem.*, 2019, **91**, 4544–4551.
9 E. Tanaka, T. Matsukawa, Y. Kuroki, M. Suzuki, K. Yokoyama and T. Hirata, *Anal. Sci.*, 2022, **38**, 695–702.
10 S. Khatib-Shahidi, M. Andersson, J. L. Herman, T. A. Gillespie and R. M. Caprioli, *Anal. Chem.*, 2006, **78**, 6448.
11 M. Shariatgorji, A. Nilsson, E. Fridjonsdottir, T. Vallianatou, P. Källback, L. Katan, J. Sävmarker, I. Mantas, X. Zhang, E. Bezard, P. Svenningsson, L. R. Odell and P. E. Andren, *Nat. Methods*, 2019, **16**, 1021–1028.
12 S. Sole-Domenech, P. Sjovall, V. Vukojevic, R. Fernando, A. Codita, S. Salve, N. Bogdanovic, A. H. Mohammed, P. Hammarstrom, K. P. R. Nilsson, F. M. LaFerla, S. Jacob, P. O. Berggren, L. Gimenez-Llort, M. Schalling, L. Terenius and B. Johansson, *Acta Neuropathol.*, 2013, **125**, 145–157.
13 D. Touboul, A. Brunelle, F. Halgand, S. De La Porte and O. Laprevote, *J. Lipid Res.*, 2005, **46**, 1388–1395.
14 L. S. Eberlin, D. R. Ifa, C. Wu and R. G. Cooks, *Angew. Chem.*, 2010, **49**, 873–876.
15 M. Shariatgorji, N. Strittmatter, A. Nilsson, P. Källback, A. Alvarsson, X. Zhang, T. Vallianatou, P. Svenningsson,

Published on 16 June 2025. Downloaded on 12/28/2025 7:27:54 PM.

R. J. A. Goodwin and P. E. Andren, *Neuroimage*, 2016, **136**, 129–138.

16 J. Zhao, J. Chen, S. Ma, Q. Liu, L. Huang, X. Chen, K. Lou and W. Wang, *Acta Pharm. Sin. B*, 2018, **8**, 320–338.

17 S. A. Iakab, P. Ràfols, X. Correig-Blanchar and M. García-Altares, *Anal. Chem.*, 2021, **93**, 6301–6310.

18 P. J. Ell, *Br. J. Radiol.*, 2006, **79**, 32–36.

19 A. W. Sauter, H. F. Wehrl, A. Kolb, M. S. Judenhofer and B. J. Pichler, *Trends Mol. Med.*, 2010, **16**, 508–515.

20 A. Matusch, L. S. Fenn, C. Depboylu, M. Klietz, S. Strohmer, J. A. McLean and J. S. Becker, *Anal. Chem.*, 2012, **84**, 3170–3178.

21 R. Masyuko, E. J. Lanni, J. V. Sweedler and P. W. Bohn, *Analyst*, 2013, **138**, 1924–1939.

22 A. Svirkova, A. Turyanskaya, L. Perneczky, C. Streli and M. Marchetti-Deschmann, *Analyst*, 2018, **143**, 2587–2595.

23 E. Lützen, M. Holtkamp, I. Stamme, R. Schmid, M. Sperling, M. Pütz and U. Karst, *Drug Test. Anal.*, 2020, **12**, 465–471.

24 J. Bianga, A. Bouslimani, N. Bec, F. Quenet, S. Mounicou, J. Szpunar, B. Bouyssiere, R. Lobinski and C. Larroque, *Metallomics*, 2014, **6**, 1382–1386.

25 R. G. de Vega, M. L. F. Sanchez, N. Eiro, F. J. Vizoso, M. Sperling, U. Karst and A. S. Medel, *Anal. Bioanal. Chem.*, 2018, **410**, 913–922.

26 P. Niehaus, R. G. de Vega, M. T. Haindl, C. Birkl, M. Leoni, A. M. Birkl-Toeglhofer, J. Haybaeck, S. Ropele, M. Seeba, W. Coessler, U. Karst, C. Langkammer and D. Clases, *Talanta*, 2024, **270**, 125518.

27 J. R. Chirinos, D. D. Oropeza, J. J. Gonzalez, H. Hou, M. Morey, V. Zorba and R. R. Russo, *J. Anal. At. Spectrom.*, 2014, **29**, 1292–1298.

28 C. Herdering, C. A. Wehe, O. Reifschneider, I. Raj, G. Ciarimboli, K. Diebold, C. Becker, M. Sperling and U. Karst, *Rapid Commun. Mass Spectrom.*, 2013, **27**, 2588–2594.

29 H. W. Paing, T. J. Bryant, C. D. Quarles, Jr. and R. K. Marcus, *Anal. Chem.*, 2020, **92**, 12622–12629.

30 L. X. Zhang and R. K. Marcus, *J. Anal. At. Spectrom.*, 2016, **31**, 145–151.

31 T. Suzuki, H. H. Khoo and T. Hirata, *Mass Spectrom.*, 2023, **12**, A0125.

32 H. H. Khoo, H. Shimada, H. Miyahara and T. Hirata, *Metallomics Research*, 2021, **1**, 44–54.

33 J. T. Shelley and G. M. Hieftje, *J. Anal. At. Spectrom.*, 2011, **26**, 2153–2159.

34 D. T. Usmanov, S. Ninomiya, L. C. Chen, S. Saha, M. K. Mandal, Y. Sakai, R. Takaishi, A. Habib, K. Hiraoka, K. Yoshimura, S. Takeda, H. Wada and H. Nonami, *Mass Spectrom.*, 2017, **6**, S0059.

35 S. K. I. Funke, V. A. Bruckel, M. Weber, E. Lutzen, J.-C. Wolf, C. Haisch and U. Karst, *Anal. Chim. Acta*, 2021, **1177**, 338770.

36 R. M. Adibhatla and J. F. Hatcher, *Future Lipidol.*, 2007, **2**, 403–422.

37 E. L. Que, D. W. Domaille and C. J. Chang, *Chem. Rev.*, 2008, **108**, 1517–1549.

38 C. Villa and J. H. Yoon, *Life*, 2021, **11**, 1202.

39 J. S. Becker, M. Zoriy, B. Wu, A. Matusch and J. S. Becker, *J. Anal. At. Spectrom.*, 2008, **23**, 1275–1280.

40 J. S. Becker, M. Zoriy, A. Matusch, B. Wu, D. Salber, C. Palm and J. S. Becker, *Mass Spectrom. Rev.*, 2010, **29**, 156–175.

41 F. C. Coelho, G. Cerchiaro, S. E. S. Araújo, J. P. L. Daher, S. A. Cardoso, G. F. Coelho and A. G. Guimarães, *Int. J. Mol. Sci.*, 2022, **23**, 7935.

42 B. O. A. Botchway, X. Liu, Y. Zhou and M. Fang, *J. Transl. Med.*, 2023, **21**, 351.

43 Y. Hirahara, T. Wakabayashi, T. Mori, T. Koike, I. Yao, M. Ysuda, K. Honke, H. Gotoh, K. Ono and H. Yamada, *J. Neurochem.*, 2017, **140**, 435–450.

44 L. Muller, K. Baldwin, D. C. Barbacci, S. N. Jackson, A. Roux, C. D. Balaban, B. E. Brinson, M. I. McCully, E. K. Lewis, J. A. Schultz and A. S. Woods, *J. Am. Soc. Mass Spectrom.*, 2017, **28**, 1716–1728.

45 T. Abe, K. Niizuma, A. Kanoke, D. Saigusa, R. Saito, A. Uruno, M. Fujimura, M. Yamamoto and T. Tominaga, *Neurol. Med.-Chir.*, 2018, **58**, 384–392.

46 Z. Yang, Z. Chang, K. Deng, J. Gu, Y. Wu, Q. Sun and Q. Luo, *Anal. Chem.*, 2023, **95**, 16786–16790.

47 W. C. Byrdwell, *Lipids*, 2001, **36**, 327–346.

48 M. Beccaria, V. Inferrera, F. Rigano, K. Gorynski, G. Purcaro, J. Pawliszyn, P. Dugo and L. Mondello, *J. Chromatogr. A*, 2017, **1509**, 69–82.

49 J.-C. Wolf, L. Gyr, M. F. Mirabelli, M. Schaer, P. Siegenthaler and R. Zenobi, *J. Am. Soc. Mass Spectrom.*, 2016, **27**, 1468–1475.

50 M. Bouza, J. Garcia-Martinez, B. Gilbert-Lopez, S. Brandt, J. F. Garcia-Reyes, A. Molina-Díaz and J. Franzke, *Anal. Chem.*, 2023, **95**, 854–861.

51 S. E. Hancock, M. G. Freidrich, T. W. Mitchell, R. J. W. Truscott and P. L. Else, *Nutrients*, 2022, **14**, 2495.

52 A. Turyanskaya, S. Smetaczek, V. Pichler, M. Rauwolf, L. Perneczky, A. Roschger, P. Roschger, P. Wobrauschek, A. Limbeck and C. Streli, *J. Anal. At. Spectrom.*, 2021, **36**, 1512–1523.

53 L. A. McDonnell, A. can Remoortere, R. J. M. van Zeijl and A. M. Deelder, *J. Proteome Res.*, 2008, **7**, 3619–3627.

54 J. Yoo, J. Han and M. H. Lim, *RSC Chem. Biol.*, 2023, **4**, 548–563.

55 P. Nemes, A. S. Woods and A. Vertes, *Anal. Chem.*, 2010, **82**, 982–988.

56 M. Perry, Q. Li and R. T. Kennedy, *Anal. Chim. Acta*, 2009, **653**, 1–22.